Geophys. J. Int. (1999) **139,** 345–358

Simulation of the spontaneous growth of a dynamic crack without constraints on the crack tip path

Nobuki Kame* and Teruo Yamashita

Earthquake Research Institute, University of Tokyo, 1-1-1 *Yayoi, Bunkyo-ku, Tokyo* 113-0032, *Japan.*

Accepted 1999 June 7. Received 1999 June 4; in original form 1998 December 15

SUMMARY

The spontaneous growth of a dynamic in-plane shear crack is simulated using a newly developed method of analysis in which no *a priori* constraint is required for the crack tip path, unlike in other classical studies. We formulate the problem in terms of boundary integral equations; the hypersingularities of the integration kernels are removed by taking the finite parts. Our analysis shows that dynamic crack growth is spontaneously arrested soon after the bending of the crack tips, even in a uniformly stressed medium with homogeneously distributed fracture strengths. This shows that the dynamics of crack growth has a significant effect on forming the non-planar crack shape, and consequently plays an essential role in the arrest of earthquake rupturing.

Key words: cracks, elastodynamics, fractures, rupture propagation.

INTRODUCTION

The analysis of the spontaneous growth of a shear crack is one of the most important problems in seismology because it helps us to predict the entire rupture process of a forthcoming earthquake. Numerous studies, both theoretical and numerical, have been made for spontaneous crack growth. For example, the dynamics of a 2-D semi-infinite shear crack was first analysed theoretically by Kostrov (1966), while numerical analyses were required for 2-D or 3-D cracks with finite extent (e.g. Das & Aki 1977a,b; Miyatake 1980a,b; Das 1981; Virieux & Madariaga 1982). A planar crack shape was implicitly assumed in these classical studies, mainly for mathematical simplicity.

However, theoretical solutions for dynamic crack growth imply crack bending at a high crack tip velocity. Yoffe (1951) and Freund (1990) pointed out that the maximum hoop traction axis shifts from the original crack plane if the crack tip velocity exceeds a certain critical value; the hoop traction is defined as the traction on an inclined plane around the crack tip (see Fig. 1). This suggests the possibility of crack bending for a fast growing crack. Indeed, it is sometimes observed that surface traces of actual faults are bent near their ends (Matsuda 1967; Kanamori 1972). Hence the assumption of a planar crack shape in the classical studies is dubious, and its validity should be investigated.

* Now at: Department of Earth and Planetary Sciences, Faculty of Science, Kyushu University, 6-10-1 Hakozaki, Higashi-ku, Fukuoka 812-8581, Japan. E-mail: kame@geo.kyushu-u.ac.jp

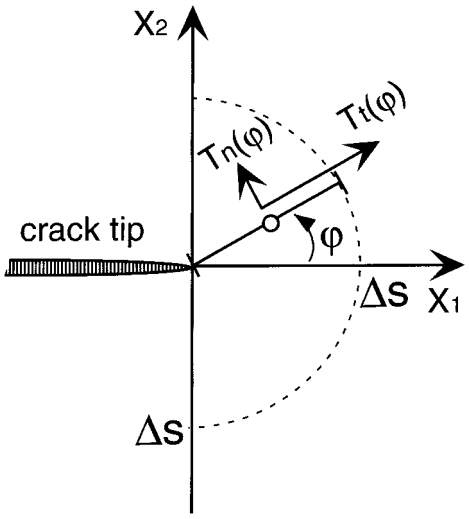

Figure 1. Hoop shear $T_t(\varphi)$ and hoop normal $T_n(\varphi)$ tractions: they act on an inclined plane originating from a crack tip. The angle φ is measured from the X_1-axis. The open circle represents a traction evaluation point in the numerical scheme. Δs is a unit length of the discrete boundary element.

Our aim here is to investigate the dynamics of a spontaneously propagating crack and its effect on the formation of crack trace geometry. It should be noted that previous studies of 2-D non-planar crack growth had limitations because of some of the underlying constraints in their numerical schemes.

One example is the need to prescribe the rupture trace prior to the dynamic nucleation. Inoue & Miyatake (1995) dealt with a curved fault (mode II) using the finite difference method (FDM) by arranging curved grids along the prescribed fault. Tada & Yamashita (1997) calculated the dynamic rupture propagation on a prescribed hackly-shaped crack using the boundary integral equation method (BIEM) for each mode of 2-D problem. Neither of these two schemes is suitable for our purposes. Another constraint appears in the study of Xu & Needleman (1994), who calculated the spontaneous crack bifurcations using the finite element method (FEM). They selected well arranged elements and node connections in the finite element discretization. Their method can begin the calculation without prescribed crack geometry, but with the restriction that the crack tip growth is only in the directions 0° and $\pm 45^\circ$ in the Cartesian coordinate system. Their concern is 2-D tensile (mode I) crack growth subject to sudden tensile loading. However, these restricted growth directions are too coarse for the representation of the boundary condition in the mode II case, as discussed in Appendix D. Thus their scheme is not useful for our purpose either. To our knowledge, the scheme of BIEM developed by Seelig & Gross (1997) can only deal with arbitrarily curvilinear dynamic crack growth. Their main concern is, however, 2-D tensile cracking, and shear crack growth has not been investigated well.

In this paper, we develop a new method to compute the spontaneous shear crack propagation without any *a priori* assumptions about its path. The time-domain BIEM is used for the formulation of an in-plane shear (mode II) crack located in an infinite homogeneous isotropic elastic medium. The BIEM is clearly flexible in formulating an arbitrary crack geometry. The boundary integral equation we used here, however, has hypersingularities (Kostrov & Das 1988; Martin & Rizzo 1989), which means that the BIEM is not immediately suited to numerical implementation: the flexibility is limited because the hypersingular integrals have to be evaluated. It will be shown that this difficulty can be overcome by taking finite parts in the hypersingular integrals. Our technique is independent of the crack geometry, so that spontaneous crack growth is easily studied without assuming the crack shape *a priori*. We simulate the spatiotemporal evolution of spontaneous crack growth using this technique. The crack tip is assumed to extend in the direction where the hoop shear traction takes the maximum value and exceeds the fracture threshold. When cracks are planar, the criterion is reduced to the shear stress fracture criterion commonly assumed in many classical studies (e.g. Das & Aki 1977b). It will be shown in our simulation that the dynamic growth of crack tip is arrested soon after its bending even in a uniformly stressed medium with homogeneously distributed fracture strengths. This gives new insight into the arresting mechanism of earthquake faulting.

HYPERSINGULAR BIEM FOR CRACK ANALYSIS

We begin with the dynamic representation theorem which expresses the elastic displacement field over the entire medium in terms of the slip distibution along a crack in an infinite homogeneous isotropic elastic 2-D medium (e.g. Aki & Richards 1980). Assuming that the medium is at rest with no slip for time $t \leq 0$ and also that the traction is continuous across the crack, we have

$$u_k(\mathbf{x}, t) = -\text{p.f.} \int_\Gamma d\xi \int_0^t d\tau \Delta u_i(\xi, \tau) c_{ijpq} n_j(\xi) \frac{\partial}{\partial x_q} \times G_{kp}(\mathbf{x}, t-\tau; \mathbf{y}(\xi), 0), \quad (1)$$

where $u_k(\mathbf{x}, t)$ is the displacement in the kth direction at position $\mathbf{x}$ and time t, Γ is the whole length of the crack trace, ξ is the arc length along Γ, $\Delta u_i(\xi, \tau)$ is the slip on the crack in the ith direction at arc length ξ and time τ, c_{ijpq} are elastic constants, $\mathbf{n}(\xi)$ is the unit vector normal to the crack trace at arc length ξ that points to the left when seen along the direction of increasing ξ, $\mathbf{y}(\xi)$ is the location of the position on the crack at arc length ξ, $G_{kp}(\mathbf{x}, t-\tau; \mathbf{y}, 0)$ is the displacement Green's function denoting the displacement in the kth direction observed at position $\mathbf{x}$ and time $t-\tau$ due to a unit force in the pth direction applied at position $\mathbf{y}$ and time 0, and summation over repeated indices is implied (Fig. 2). Here the kernel functions $\partial G_{kp}/\partial x_q$ contain hypersingularities and p.f. stands for taking a finite part of the divergent integral; the details will be given in Appendix B.

Application of Hooke's law leads to the following representation for stresses in the full space:

$$\sigma_{kl}(\mathbf{x}, t) = \frac{1}{2} c_{klrs} \left(\frac{\partial u_s}{\partial x_r} + \frac{\partial u_r}{\partial x_s} \right) = -\text{p.f.} \int_\Gamma d\xi \int_0^t d\tau \Delta u_i(\xi, \tau) c_{ijpq} n_j(\xi) \frac{\partial}{\partial x_q} \times \Sigma_{klp}(\mathbf{x}, t-\tau; \mathbf{y}(\xi), 0), \quad (2)$$

where

$$\Sigma_{ijk}(\mathbf{x}, t-\tau; \mathbf{y}, 0) \equiv c_{ijpq} \frac{\partial}{\partial x_q} G_{pk}(\mathbf{x}, t-\tau; \mathbf{y}, 0) \quad (3)$$

is the stress Green's function denoting the ij-component of the stress observed at position $\mathbf{x}$ and time $t-\tau$ due to a unit force in the kth direction applied at position $\mathbf{y}$ and time 0. The integrand in eq. (2) has stronger singularities than in eq. (1) because of the spatial differentiation.

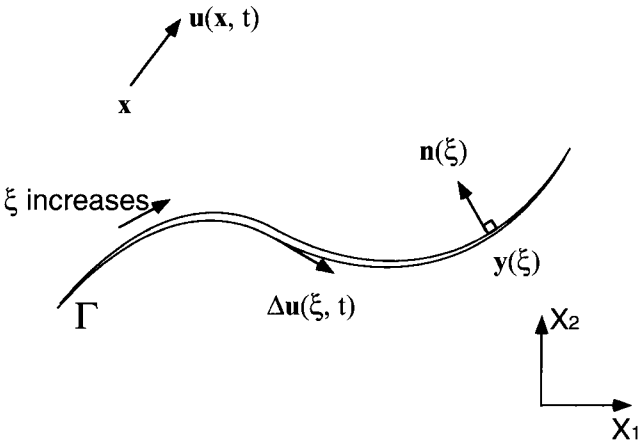

Figure 2. Nomenclature used in the crack analysis.

In the 2-D in-plane shear crack problem to be treated in this paper, we assume that the crack surface is closed everywhere, or that the displacement discontinuity on the crack has only a tangential (purely mode II) component. Denoting the amount of right-lateral shear slip by Δu_t, we obtain the relations

$$\begin{cases} \Delta u_1(\xi,\tau) = n_2(\xi)\Delta u_t(\xi,\tau), \\ \Delta u_2(\xi,\tau) = -n_1(\xi)\Delta u_t(\xi,\tau). \end{cases} \tag{4}$$

Using the above notation, we have

$$\begin{aligned} u_1(\mathbf{x},t) = &-\text{p.f.}\int_\Gamma d\xi \int_0^t d\tau \\ &\times \left\{ [\Delta u_1(\xi,\tau)(\lambda+2\mu)n_1(\xi) + \Delta u_2(\xi,\tau)\lambda n_2(\xi)]\frac{\partial}{\partial x_1}G_{11} \right. \\ &+ [\Delta u_1(\xi,\tau)\lambda n_1(\xi) + \Delta u_2(\xi,\tau)(\lambda+2\mu)n_2(\xi)]\frac{\partial}{\partial x_2}G_{12} \\ &+ [\Delta u_1(\xi,\tau)\mu n_2(\xi) + \Delta u_2(\xi,\tau)\mu n_1(\xi)] \\ &\left. \times \left(\frac{\partial}{\partial x_2}G_{11} + \frac{\partial}{\partial x_1}G_{12}\right)\right\} \\ = &-\text{p.f.}\int_\Gamma d\xi \int_0^t d\tau \Delta u_t(\xi,\tau)\mu \\ &\times \left\{ 2n_1(\xi)n_2(\xi)\left(\frac{\partial}{\partial x_1}G_{11} - \frac{\partial}{\partial x_2}G_{12}\right)\right. \\ &\left. + [n_2^2(\xi) - n_1^2(\xi)]\left(\frac{\partial}{\partial x_2}G_{11} + \frac{\partial}{\partial x_1}G_{12}\right)\right\} \\ = &-\int_\Gamma d\xi \int_0^t d\tau \Delta \dot{u}_t(\xi,\tau)\mu \\ &\times \left\{ 2n_1(\xi)n_2(\xi)\left(\frac{\partial}{\partial x_1}R_{11} - \frac{\partial}{\partial x_2}R_{12}\right)\right. \\ &\left. + [n_2^2(\xi) - n_1^2(\xi)]\left(\frac{\partial}{\partial x_2}R_{11} + \frac{\partial}{\partial x_1}R_{12}\right)\right\}, \end{aligned} \tag{5}$$

$$\begin{aligned} u_2(\mathbf{x},t) = &-\int_\Gamma d\xi \int_0^t d\tau \Delta \dot{u}_t(\xi,\tau)\mu \\ &\times \left\{ 2n_1(\xi)n_2(\xi)\left(\frac{\partial}{\partial x_1}R_{21} - \frac{\partial}{\partial x_2}R_{22}\right)\right. \\ &\left. + [n_2^2(\xi) - n_1^2(\xi)\left(\frac{\partial}{\partial x_2}R_{21} + \frac{\partial}{\partial x_1}R_{22}\right)\right\}, \end{aligned} \tag{6}$$

where the displacement field is represented in terms of the slip velocity $\dot{u}_t(\xi,\tau)$ by way of integration by parts in terms of τ. The Green's function $G(\tau)$ is then integrated to give $R(\tau) \equiv \int_0^\tau G(t)dt$, where $R(\tau)$ means the Heaviside step response. Hypersingularities disappear in eqs (5) and (6) as a result of the integration.

Likewise, the stress field is expressed in terms of the slip velocity:

$$\begin{aligned} &\frac{1}{2}[\sigma_{11}(\mathbf{x},t) - \sigma_{22}(\mathbf{x},t)] \\ &= -\text{p.f.}\frac{1}{2}\int_\Gamma d\xi \int_0^t d\tau \Delta u_t(\xi,\tau)\mu \left\{ [n_2^2(\xi) - n_1^2(\xi)] \right. \\ &\quad \times \left(\frac{\partial}{\partial x_2}\Sigma_{111} + \frac{\partial}{\partial x_1}\Sigma_{112} - \frac{\partial}{\partial x_2}\Sigma_{221} - \frac{\partial}{\partial x_1}\Sigma_{222}\right) \\ &\quad + 2n_1(\xi)n_2(\xi) \\ &\quad \left. \times \left(\frac{\partial}{\partial x_1}\Sigma_{111} - \frac{\partial}{\partial x_2}\Sigma_{112} - \frac{\partial}{\partial x_1}\Sigma_{221} + \frac{\partial}{\partial x_2}\Sigma_{222}\right)\right\} \\ &= -\text{p.f.}\int_\Gamma d\xi \int_0^t d\tau \Delta u_t(\xi,\tau)\mu^2 \left\{ [n_2^2(\xi) - n_1^2(\xi)] \right. \\ &\quad \times \left[\frac{\partial^2}{\partial x_1 \partial x_2}(G_{11} - G_{22}) + \left(\frac{\partial^2}{\partial x_1^2} - \frac{\partial^2}{\partial x_2^2}\right)G_{12}\right] \\ &\quad \left. + 2n_1(\xi)n_2(\xi)\left(\frac{\partial^2}{\partial x_1^2}G_{11} + \frac{\partial^2}{\partial x_2^2}G_{22} - 2\frac{\partial^2}{\partial x_1 \partial x_2}G_{12}\right)\right\} \\ &= -\text{p.f.}\int_\Gamma d\xi \int_0^t d\tau \Delta \dot{u}_t(\xi,\tau)\mu^2 \left\{ [n_2^2(\xi) - n_1^2(\xi)] \right. \\ &\quad \times \left[\frac{\partial^2}{\partial x_1 \partial x_2}(R_{11} - R_{22}) + \left(\frac{\partial^2}{\partial x_1^2} - \frac{\partial^2}{\partial x_2^2}\right)R_{12}\right] \\ &\quad \left. + 2n_1(\xi)n_2(\xi)\left(\frac{\partial^2}{\partial x_1^2}R_{11} + \frac{\partial^2}{\partial x_2^2}R_{22} - 2\frac{\partial^2}{\partial x_1 \partial x_2}R_{12}\right)\right\}, \end{aligned} \tag{7}$$

$$\begin{aligned} &\frac{1}{2}[\sigma_{11}(\mathbf{x},t) + \sigma_{22}(\mathbf{x},t)] \\ &= -\text{p.f.}\int_\Gamma d\xi \int_0^t d\tau \Delta \dot{u}_t(\xi,\tau)\mu(\lambda+\mu) \left\{ [n_2^2(\xi) - n_1^2(\xi)] \right. \\ &\quad \times \left[\frac{\partial^2}{\partial x_1 \partial x_2}(R_{11} + R_{22}) + \left(\frac{\partial^2}{\partial x_1^2} + \frac{\partial^2}{\partial x_2^2}\right)R_{12}\right] \\ &\quad \left. + 2n_1(\xi)n_2(\xi)\left(\frac{\partial^2}{\partial x_1^2}R_{11} - \frac{\partial^2}{\partial x_2^2}R_{22}\right)\right\}, \end{aligned} \tag{8}$$

$$\begin{aligned} \sigma_{12}(\mathbf{x},t) = &-\text{p.f.}\int_\Gamma d\xi \int_0^t d\tau \Delta \dot{u}_t(\xi,\tau)\mu^2 \left\{ [n_2^2(\xi) - n_1^2(\xi)] \right. \\ &\times \left(\frac{\partial^2}{\partial x_2^2}R_{11} + \frac{\partial^2}{\partial x_1^2}R_{22} + 2\frac{\partial^2}{\partial x_1 \partial x_2}R_{12}\right) + 2n_1(\xi)n_2(\xi) \\ &\left. \times \left[\frac{\partial^2}{\partial x_1 \partial x_2}(R_{11} - R_{22}) + \left(\frac{\partial^2}{\partial x_1^2} - \frac{\partial^2}{\partial x_2^2}\right)R_{12}\right]\right\}, \end{aligned} \tag{9}$$

where λ and μ are the Lamé constants and the identity

$$G_{12} = G_{21} \tag{10}$$

was used. The rewriting of the stress in terms of the slip velocity has an advantage in solving dynamic crack problems in that a change in the slip velocity is directly associated with a traction change on a crack (Cochard & Madariaga 1994). As noted in the preceding section, the integral representations (eqs 7, 8 and 9) contain hypersingularities that cannot be discretized directly.

With the limiting process $\mathbf{x} \to \mathbf{y}(s)$, we obtain, for the shear traction $T_t(s, t)$ on the crack at arc length s and time t,

$$T_t(s,t) = 2n_1(s)n_2(s)\frac{1}{2}[\sigma_{11}(\mathbf{y}(s),t) - \sigma_{22}(\mathbf{y}(s),t)] + [n_2^2(s) - n_1^2(s)]\sigma_{12}(\mathbf{y}(s),t). \quad (11)$$

This is the hypersingular integral equation that express the traction on the crack in terms of the slip velocity on it.

Likewise, the normal traction $T_n(s, t)$ across the crack at arc length s and time t is given by

$$T_n(s,t) = \frac{1}{2}[\sigma_{11}(\mathbf{y}(s),t) + \sigma_{22}(\mathbf{y}(s),t)] - [n_2^2(s) - n_1^2(s)]\frac{1}{2}[\sigma_{11}(\mathbf{y}(s),t) - \sigma_{22}(\mathbf{y}(s),t)] + 2n_1(s)n_2(s)\sigma_{12}(\mathbf{y}(s),t). \quad (12)$$

The 2-D Green's functions are given in Appendix A.

NUMERICAL IMPLEMENTATION

For the sake of the numerical implementation, the crack trace is approximated by an open polygon consisting of m elements of constant length Δs and nodal points $y(i\Delta s)(i = 1, 2, \ldots, m+1)$. The number of crack elements m increases with time since crack growth is modelled by adding new elements to the moving crack tips. Time t is also discretized by a set of equally spaced time steps with an interval of Δt.

The slip velocity is interpolated by a piecewise constant function that is assumed to be constant over an element and discontinuous between elements (e.g. Cochard & Madariaga 1994; Fukuyama & Madariaga 1998):

$$\Delta\dot{u}(s,t) = \sum_i \sum_k V^{i,k}\phi^i(s)\theta^k(t), \quad (13)$$

with

$$\phi^i(s) \equiv \begin{cases} 1 & \text{if } s^i < s < s^{i+1} \\ 0 & \text{otherwise} \end{cases} \quad (14)$$

$$\theta^k(t) \equiv \begin{cases} 1 & \text{if } t^{k-1} < t < t^k \\ 0 & \text{otherwise}, \end{cases} \quad (15)$$

where $\phi^i(s)$ and $\theta^k(t)$ are the spatial and temporal interpolation functions with $s^i \equiv i\Delta s$ and $t^k \equiv k\Delta t$ respectively, and $V^{i,k}$ is the discretized slip velocity at the kth time step on the ith element (see Fig. 3). With the piecewise constant interpolation, each element is an independent calculation unit and no special constraint need be imposed at a junction where two or more crack elements meet.

Substituting the interpolated slip velocity distribution into the stress representations, we have the stress components written in a discrete form:

$$\sigma_{ij}(\mathbf{x}, t^n) = \text{p.f.} \int_\Gamma \int_0^t \Delta\dot{u}_t(\xi,\tau)\frac{\partial^2}{\partial x_p \partial x_q} R d\xi\, d\tau = \sum_{k=1}^{n}\sum_{i}^{m} V^{i,k}\,\text{p.f.} \int_{s_i}^{s_{i+1}} \int_{t_{k-1}}^{t_k} \frac{\partial^2}{\partial x_p \partial x_q} R\, d\xi\, d\tau = \sum_{k=1}^{n}\sum_{i}^{m} V^{i,k} I^{i,k-n}(\mathbf{x}), \quad (16)$$

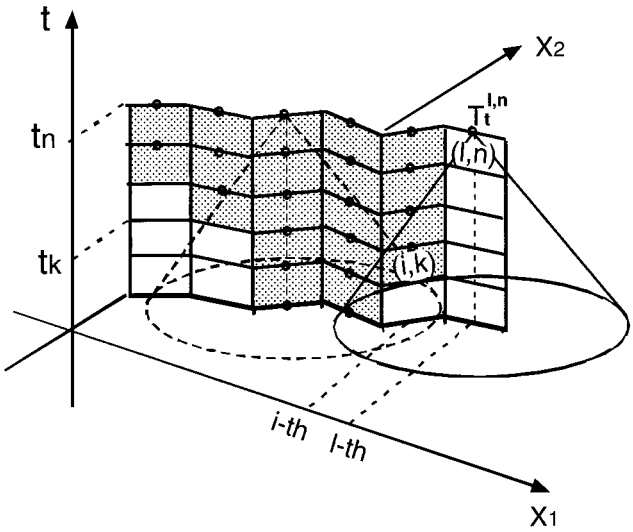

Figure 3. Schematic diagram of the discretized BIEM. Grey elements represent those that have non-zero slip velocity.

where we abbreviate the elastic moduli and the normal vectors that are different among the components. While the observation time t^n is discontinuous in the above formulation, the observation point $\mathbf{x}$ is still continuous. This property will be used in calculating the angular distribution of hoop traction around the crack tips. $I^{i,k-n}(\mathbf{x})$ is the discretized stress operator, which represents the contribution of a unit slip velocity to the stress at the observation position $\mathbf{x}$ and time t^n:

$$I^{i,k-n}(\mathbf{x}) = \text{p.f.} \int_{s_i}^{s_{i+1}} \int_{t_{k-1}}^{t_k} \frac{\partial^2}{\partial x_p \partial x_q} R\, d\xi\, d\tau. \quad (17)$$

Spatiotemporal convolution in eq. (17) has to be calculated inside the wave cones that satisfy the causality functions $H(t^n - \tau - r/\alpha)$ or $H(t^n - \tau - r/\beta)$ of the Green's functions, and the singularities appear at the wavefronts $(t^n - \tau) - r/\alpha = 0$ and $(t^n - \tau) - r/\beta = 0$, where

$$r \equiv \sqrt{[x_1 - y_1(\xi)]^2 + [x_2 - y_2(\xi)]^2}$$

is the distance between the observation point and the source point (see Fig. 2). α and β represent the P- and S-wave velocities of the medium, respectively.

Our definition of the finite part enables us to evaluate the hypersingular integral $I^{i,k-n}(\mathbf{x})$ analytically in terms of only the primitive functions without any numerical integrations (see Appendix B). This is a major advantage of the finite part method used in the paper.

By constructing the shear traction $T_t^{l,n}$ from the stress components $\sigma_{ij}^{l,n} = \sigma_{ij}((s^l)', t^n)$, the boundary integral eq. (11) is reduced to a set of simultaneous linear algebraic equations:

$$T_t^{l,n} = \sum_{k=1}^{n}\sum_{i}^{m} V^{i,k} K^{l-i,n-k}, \quad (18)$$

where K is the total sum of the discretized stress components and the traction is evaluated at the mid-point of each crack element, $(s^l)' = s^l + \Delta s/2$.

Eq. (18) gives the solution for the slip velocity in the time stepping scheme:

$$V^{l,n} = \frac{T_t^{l,n}}{K^{0,0}} - \frac{1}{K^{0,0}} \sum_{k}^{n-1} \sum_{i}^{m} V^{i,k} K^{l-i,n-k}. \quad (19)$$

The slip velocity $V^{l,n}$, unknown at the current time t^n, can be computed by eq. (19), which includes a contribution from the past velocity ($k = 1, 2, \ldots, n-1$) and the current shear traction $T_t^{l,n}$:

$$T_t^{l,n} = -\Delta\sigma^{l,n}, \quad (20)$$

where $\Delta\sigma^{l,n}$ is the shear stress drop on the element that is given as the boundary condition.

Our numerical computations are made using the following non-dimensional quantities:

$$T_t' = T_t/\mu, \qquad V' = V/\alpha, \qquad x' = x/\Delta s, \qquad t' = t\alpha/\Delta x. \quad (21)$$

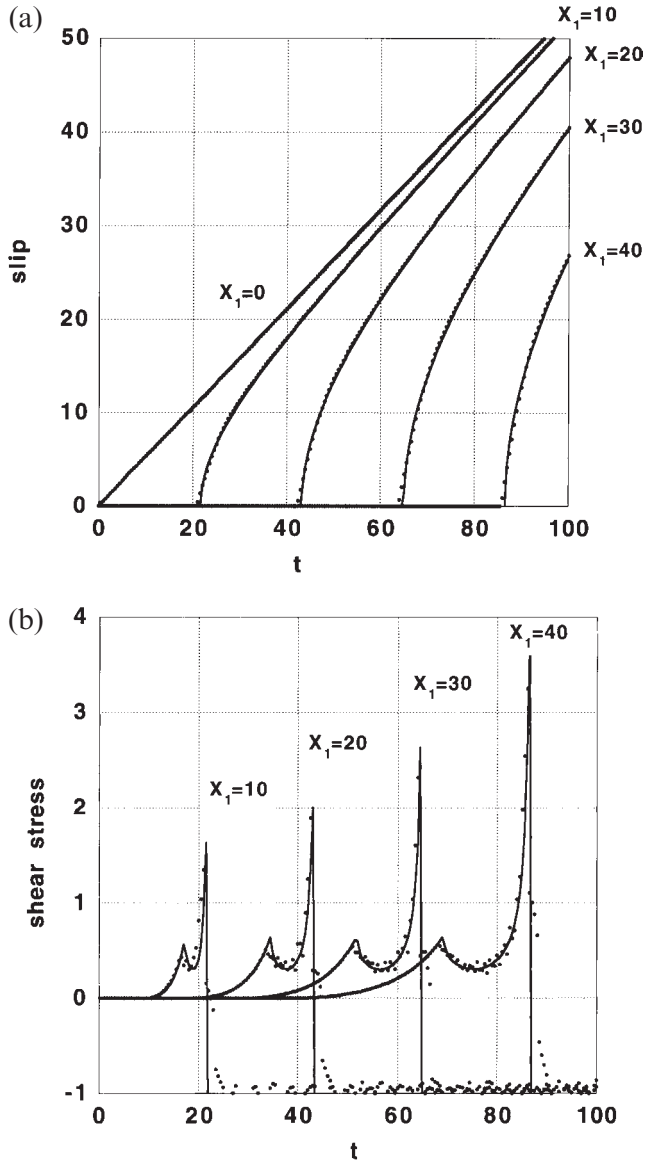

Figure 4. Comparison of the numerical and analytical solutions for the self-similar dynamic crack growth problem (e.g. Kostrov 1964; Freund 1990) for (a) time evolution of the slip Δu_1 and (b) time evolution of the stress σ_{12}. The dots denote the numerical results with an adequate damping coefficient. The solid lines represent the analytical solutions.

We assume $\alpha/\beta = \sqrt{3}$, ($\lambda = \mu$), a Poissonian solid. These non-dimensional quantities are equivalent to assuming that $\mu = 1$, $\alpha = 1$, $\beta = 1/\sqrt{3}$, $\Delta s = 1$. We choose the discretization intervals so that $\alpha\Delta t/\Delta s = 0.5$. The prime symbol is omitted in the following for simplicity.

COMPARISON WITH THE ANALYTICAL SOLUTION

Our method of analysis is corroborated by comparing the numerical solution for the self-similar crack growth problem with the analytical one. An exact analytical solution for dynamically propagating cracks with finite extent is available only for the self-similar crack problem, where a straight crack begins to form at the instant $t = 0$ and then propagates along the X_1-axis on the X_1X_2-plane bilaterally from the origin with a fixed rupture velocity. The stress drop is assumed to be constant ($\Delta\sigma = 1$) everywhere on the crack plane. The method of solution for this class of self-similar problem has been discussed in numerous references including Kostrov (1964) and Freund (1990).

In the time-marching numerical modelling of propagating cracks, short-wavelength oscillations in slip velocity become evident due to the discrete progresses of the fracture front along the discretized surface, and this leads to numerical instabilities. In order to suppress such numerical instabilities that evolve with time, artificial damping is introduced, as in previous studies (Yamashita & Fukuyama 1996; Kame & Yamashita 1997; Tada & Yamashita 1997).

Fig. 4 shows the numerical and analytical solutions. The slip Δu_1 and the stress σ_{12} are shown at several positions along the X_1-axis as a function of time. The continuous lines show the exact analytical solutions, while the dots represent the

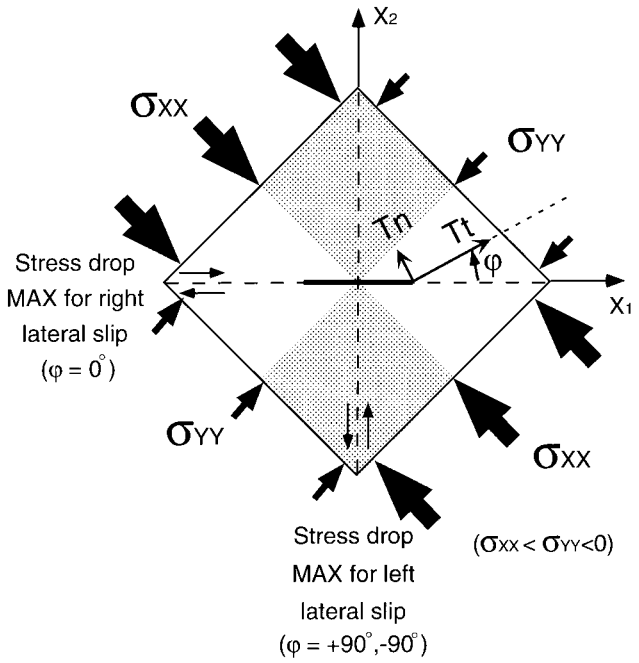

Figure 5. The configuration of the model. We assume a seed crack with right-lateral slip along the X_1-axis where the maximum stress drop occurs.

numerical ones. The numerical solution for the slip follows the analytical solution very closely: it is zero before the arrival of the rupture front and then increases hyperbolically as predicted by the theoretical result (Fig. 4a). The stress is also modelled very well by the numerical solution (Fig. 4b). In particular, the peak associated with the S wave is well represented in the numerical result. It should be noted that the peak does not appear in the classical FDM treatment (Virieux & Madariaga 1982) because such a FDM inevitably includes numerical dispersion and is therefore inadequate for representing an impulsive waveform: recent work on a fourth-order staggered grid FDM, however, improved the numerical implementation and calculated the peak (Madariaga *et al.* 1998). It is now confirmed that the numerical results are in good quantitative agreement with the analytical solutions, provided that the artificial damping coefficient C (following the notation of Tada & Yamashita 1997) takes an adequate value, which is assumed to be 0.5 throughout our calculations. The stress just behind the crack tip is, however, slightly disturbed by the damping, although it should satisfy $T_t = -1$ as given by the boundary condition.

THE EFFECT OF REMOTELY APPLIED STRESS AND THE PROCEDURE FOR SPONTANEOUS CRACK GROWTH

A uniform stress state caused by the remotely applied compressive stresses σ_{XX} and σ_{YY} is assumed to be a reference state, and the relative change from this state is analysed below. Shear traction is assumed to be completely released on the crack surface. No process zone is considered, and the stress suddenly drops behind the crack tips. The stress drop on the crack with right-lateral slip inclined at angle φ is given by $\Delta\sigma(\varphi) = \tau_0 \cos 2\varphi$, where $\tau_0 = (\sigma_{XX} - \sigma_{YY})/2$; the angle φ is measured from the X_1-axis (see Fig. 5).

Note that the stress drop becomes negative for cracks whose inclination angle φ is in the range $45^\circ < |\varphi| < 135^\circ$ because left-lateral slip is expected to release the shear traction there.

We employ a hoop shear maximization criterion similar to that in Koller *et al.* (1992) as a criterion for crack tip extension. At the nth time step, the angular distribution of hoop shear traction $T_t(\varphi_n)$ is calculated ahead of the crack tip in the range

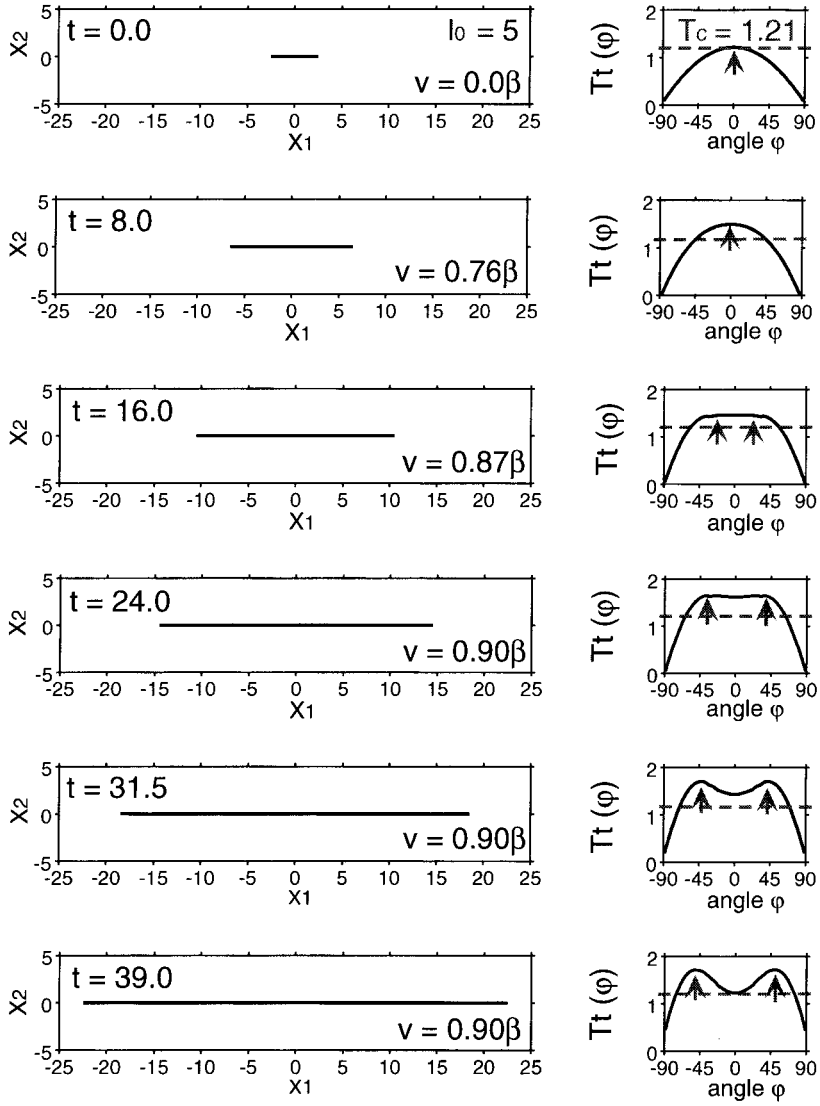

Figure 6. Snapshots of model A. The right column represents the angular distribution of the hoop shear traction corresponding to the left column. The arrows indicate the angles of the maximum hoop shear tractions.

$\varphi_{n-1} - 90^\circ < \varphi_n < \varphi_{n-1} + 90^\circ$ every 1°, where φ_{n-1} is the crack tip angle at the preceding time step. The crack tip angle is now defined as the inclination of the crack tip element measured from the X_1-axis. The traction evaluation point is $\Delta s/2$ ahead of the tip; that is, at the mid-point of the forthcoming crack element (see Fig. 1). Then we search for the maximum value $T_t(\varphi'_n)$ and its direction φ'_n. If $T_t(\varphi'_n)$ exceeds the critical fracture strength of the medium T_c, the tip is assumed to extend by 1 element in the direction φ'_n.

A static seed crack with right-lateral slip is assumed on the plane $\varphi = 0^\circ$, where the maximum shear stress drop occurs. Using elastostatic BIEM, we first determine the static slip distribution on the seed crack that is in a state of equilibrium (see Appendix C) and then calculate the stress concentration at the tip. We assume a fracture strength T_c that is slightly smaller than the shear traction at the tip of the seed crack to nucleate the dynamic growth. The nucleation is assumed to occur at $t = 0$. When a seed crack is introduced, we change eq. (19) slightly to take the static slip D^i into account:

$$V^{l,n} = -\frac{\Delta\sigma^{l,n}}{K^{0,0}} - \frac{1}{K^{0,0}}\left(\sum_{k=1}^{n-1}\sum_{i}^{m} V^{i,k}K^{l-i,n-k} + \sum_{i}^{m_0} D^i K^{l-1}_{\text{static}}\right), \tag{22}$$

where m_0 represents the number of elements making up the seed crack. Note that unless the crack tip propagates for $t \geq 0$, eq. (22) gives zero slip velocity over the seed crack.

SIMULATION OF SPONTANEOUS CRACK GROWTH

We now investigate the trace of a spontaneously growing shear crack using our newly developed method of analysis. We assume the ideal conditions that the fracture parameters, τ_0 and T_c, are homogeneously distributed over the medium. Due to the conditions without any inhomogeneities, we can elicit the effect of dynamics on the spatiotemporal evolution of the crack trace. The initial length of the seed crack is assumed to be $l_0 = 5$ and the critical fracture strength is correspondingly determined to be $T_c = 1.21$. We also assume $\tau_0 = 1$ for the stress drop function $\Delta\sigma(\varphi)$.

As a reference, we first investigate spontaneous crack growth in a classical way, where a planar crack shape had been assumed implicitly; this is termed model A. In this model, the crack tip angle is fixed at $\varphi = 0^\circ$ during the growth, and the stress drop is therefore constant over the planar crack surface. In this classical model, the time evolution of the crack tip velocity and that of the hoop shear distribution are calculated. The left column of Fig. 6 shows snapshots of the spontaneous crack growth. After dynamic nucleation at $t = 0.0$, the crack tip velocity v rapidly increases ($t = 8.0$, $t = 16.0$) and after a while reaches an upper limit of $v = 0.90\beta$ ($t = 24.0$, $t = 31.5$, $t = 39.0$). As the crack tip extensions occur in a discrete way, we arbitrarily define the numerical crack tip velocity as a spatiotemporally averaged value: we take seven neighbouring crack elements and count the time steps during which the rupture front passes through them. The crack growth continues and never stops for a homogeneous distribution of T_c and τ_0, as we have seen in the classical analyses (e.g. Das & Aki 1977b). We also calculate the angular distribution of hoop shear traction at the tip of the growing planar crack. The right column of Fig. 6 shows snapshots of the hoop shear traction at times corresponding to those in the left column. The result indicates that the axis of the maximum hoop shear traction tends to shift from the original plane as the crack tip velocity increases. This property of rapidly growing crack was first pointed out by Yoffe (1951), who obtained the analytical expression for the singular stress field around a mode I crack tip. Freund (1990) derived the singular terms at the growing crack tip for all fracture modes that have the same property as mode I. Our result has the same tendency as Freund's solution. Strictly speaking, we cannot exactly compare the computed hoop traction with the analytical singular term because the hoop traction we calculated includes not only the singular term but also the higher-degree terms. Koller *et al.* (1992) obtained a similar numerical result for the case of anti-plane (mode III) cracking.

It has been numerically verified above that the axis of maximum hoop shear traction shifts from the original plane. We now calculate the response of the hoop shear traction to a unit slip velocity in order to interpret the shift of the axis of maximum hoop shear traction (see Fig. 7). A unit slip velocity is given on an isolated crack elemental at time $t = 0.0$, and the hoop shear traction around the element tip is calculated for the subsequent time steps. A response first appears at $t = 0.5$, with the arrival of the stress waves emitted from the element. The maximum response at this time is in the directions $\pm 95^\circ$, behind the tip of the element, and then moves to $\pm 46^\circ$, to

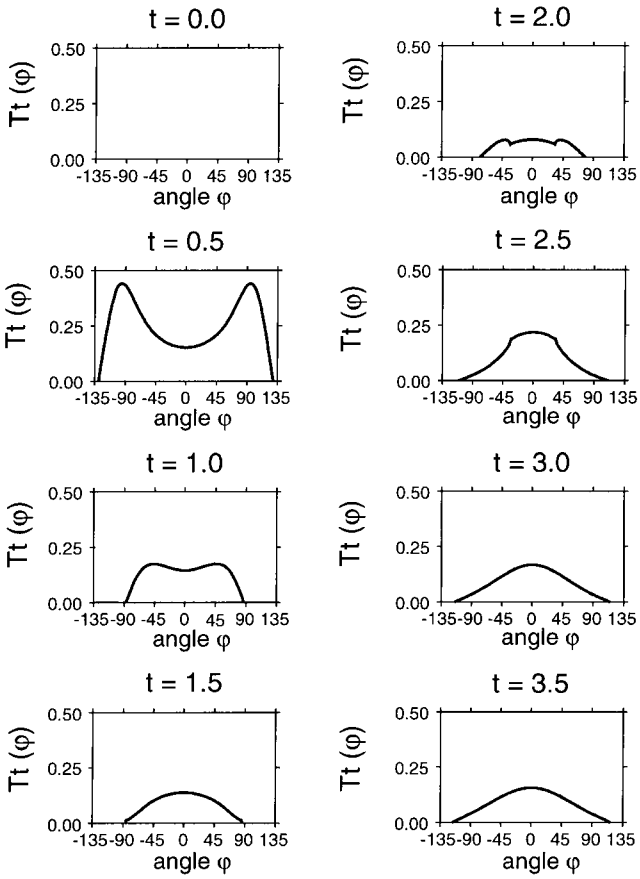

Figure 7. Snapshots of the response of the hoop shear traction to a unit slip velocity.

the front of the tip, at $t = 1.0$. After some transition period ($t = 1.5$, 2.0, 2.5), the angular distribution of the hoop shear traction becomes stable ($t = 3.0$, 3.5) and will converge to the static response, which has the maximum traction axis at $\varphi = 0°$. As shown in Fig. 7, the response is characterized by two distinct stages. The first is 'the dynamic stage' ($t = 0.5$, 1.00 during which the hoop traction is greatly affected by the stress waves, which are directly related to the slip velocity on the element. It is characterized by a short duration and non-planar ($\varphi \neq 0°$) maximum directions. After the stress waves propagate away from the tip, there is 'the static state', the behaviour of which is familiar: the hoop traction in this state is mainly formed by the static slip, not by the slip velocity, on the element, and its maximum direction is $\varphi = 0°$.

The above calculation leads us to the following conclusion: when the crack tip velocity is fairly low compared with that of the elastic waves, the stress waves emitted from the crack tip soon propagate away from the tip. Accordingly, the static effect dominates and the axis of the maximum hoop traction remains in the planar direction $\varphi = 0°$. The crack is expected to extend in a planar way at this slow propagation state. As the crack tip velocity increases, the dynamic effect begins to dominate over a certain critical velocity; the higher the crack tip velocity is, the longer the emitted stress waves stay around the tip (see Appendix D for details about the critical velocity). That is why the direction of the maximum hoop traction begins to shift from the original plane at the high-speed propagation stage and the crack tip is expected to bend.

We now carry out a simulation of spontaneous crack growth with no constraints on the crack tip path. Two models, model B and model C, are assumed in the calculations: the difference is that the crack tip bufurcation is allowed only in model B. The initial settings of model B and model C are the same as in model A.

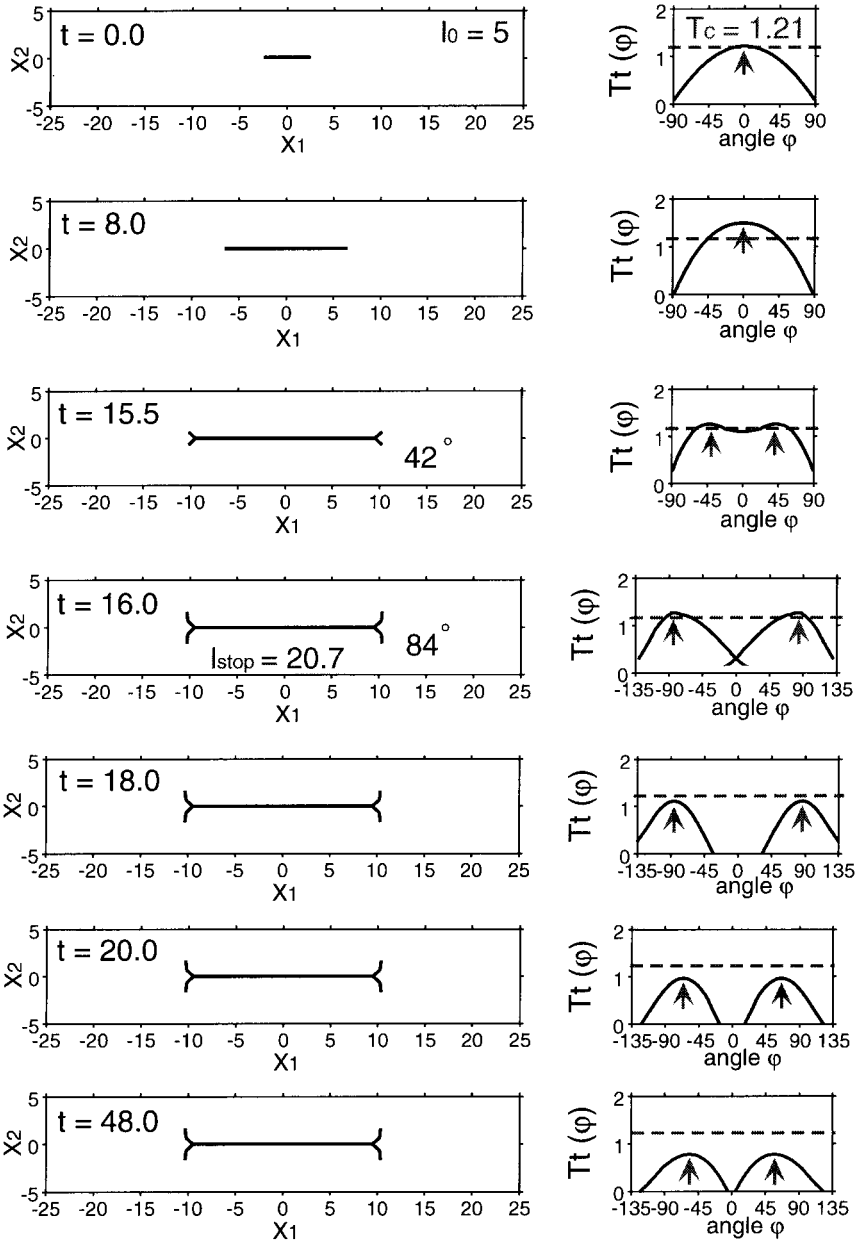

Figure 8. Snapshots of model B.

Fig. 8 shows the snapshots of the rupture growth and the corresponding hoop shear traction for model B. The shear traction is maximum in the direction of the original crack plane at $t = 0.0$; that is, the crack begins its growth along the original crack plane. The crack growth accelerates soon after the nucleation, and the crack velocity attains a value of 0.76β at $t = 8.0$. The maximum shear traction axis remains on the original crack plane, so that the crack growth continues to be straight. At $t = 15.5$, the velocity attains a value of 0.87β and the maximum shear traction exceeds the fracture strength on a plane other than the original crack plane for the first time. The directions deviate from the original crack plane by $\pm 42^\circ$. At this time step, the crack tip bifurcates into two branches spontaneously. After the bifurcation, we continue to calculate the hoop shear traction for each branch. At $t = 16.0$, the maximum tractions exceed the fracture strength in the directions $+84^\circ$ and -84° for the upper and lower branches, and the crack bending angle increases. After $t = 16.0$, the maximum shear traction never exceeds the fracture strength ($t = 18.0$, 20.0, 48.0); that is, the crack tip extension is arrested at $t = 16.0$. The final crack length is $l_{stop} = 20.7$, which is about four times as large as the initial length; l_{stop} denotes the length of the arrested crack projected onto the X_1-axis. The slip on the crack is assumed to be unlocked throughout our analyses. If the swinging back of the slip is prohibited on the crack, the final slip distribution will certainly differ from that of model B. Self-arresting of the crack tip extension is, however, still expected to occur in that case because the locking of the slip occurs only after the arrest of crack tip growth.

In model C, crack bifurcation is assumed to be prohibited, but the crack is allowed to grow in any direction. The snapshots are shown in Fig. 9. The crack tip accelerates monotonically as observed in model B. At $t = 15.5$, the velocity attains a value of 0.87β and the maximum shear traction again exceeds the fracture strength not on the original crack plane but on the plane $\pm 42^\circ$. Here the crack is assumed to bend in the direction of -42°, taking account of the effect of virtual friction. The crack generates compressive and tensile tractions in the regions marked with plus and minus symbols, respectively (see Fig. 9). It is expected that slip occurs more easily in the tensile stress regime than in the compressive one. It is therefore reasonable to assume crack growth in the direction of -42°. The crack bending increases with the growth, as seen in the snapshots at $t = 16.5$ and 18.0. After $t = 18.0$, the maximum shear traction never exceeds the fracture strength, so the dynamic crack growth is arrested at this instant. The final crack length is $l_{stop} = 21.2$, which is slightly larger than that in model B: the stress concentration level at the tip decreases with the bifurcation, so dynamic growth is arrested sooner in model B than in model C. The difference between the two models, however, seems to be slight.

Contrary to the classical model A, the crack growth is spontaneously arrested even under homogeneous conditions in models B and C. The spontaneous crack arresting can be

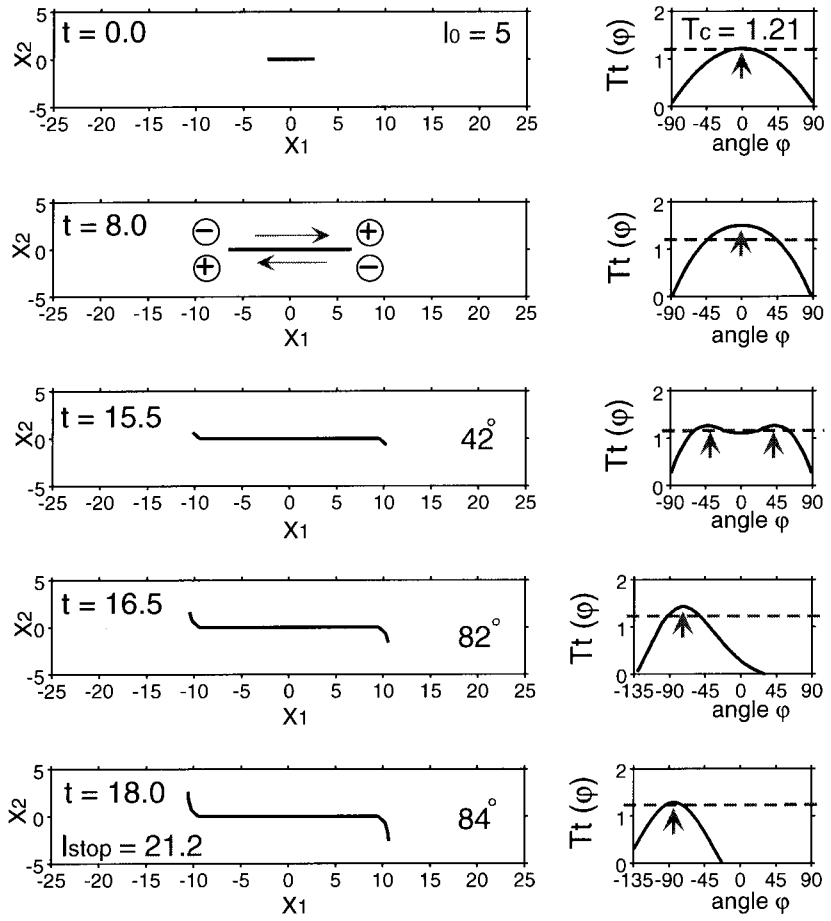

Figure 9. Snapshots of model C.

interpreted as follows: once the crack begins bending, the crack tips' angles increase with growth and the tips finally enter regions where the shear traction to be released on the crack is negative (see Fig. 5). This causes a significant reduction of stress concentration at the tips, and the stress concentration level falls short of the fracture strength. As shown above, the bending of the crack tip plays a crucial role in the arresting of earthquake rupturing. This is peculiar to shear cracking; as shown in Appendix D, the negative stress drop does not occur in tensile cracking even for steep bending.

When we make the discretization finer, crack bending becomes smoother (Fig. 10). In the finely discretized model, the initial seed crack is represented by 11 elements, which is about twice the number of elements assumed in model C. The direction of the maximum hoop shear traction is expected to change continuously, with a smooth increase of the crack tip velocity in the continuum limit. In model C, the axis of the maximum hoop traction suddenly changes direction from $\varphi = 0^\circ$ to $\varphi = 42^\circ$ due to the coarser discretization. The finer model makes an improvement at this point. The first deviation of the axis of the maximum hoop traction emerges in the direction 8°. The bent branch is finally composed of elements inclined by 8°, 28°, 57° and 77°. The final crack shapes are, however, almost independent of the discretization (see Fig. 10), so that we can conclude that the calculated result of spontaneous bending and arresting is reliable. However, we also observe that the length of the bent branch is smaller in the finely discretized model. This suggests that the crack growth will be arrested immediately after the onset of bending in the continuum limit.

CONCLUSIONS

We have successfully simulated the spontaneous growth of an in-plane shear crack with no *a priori* constraints on the crack tip path. A new efficient method of analysis has been developed

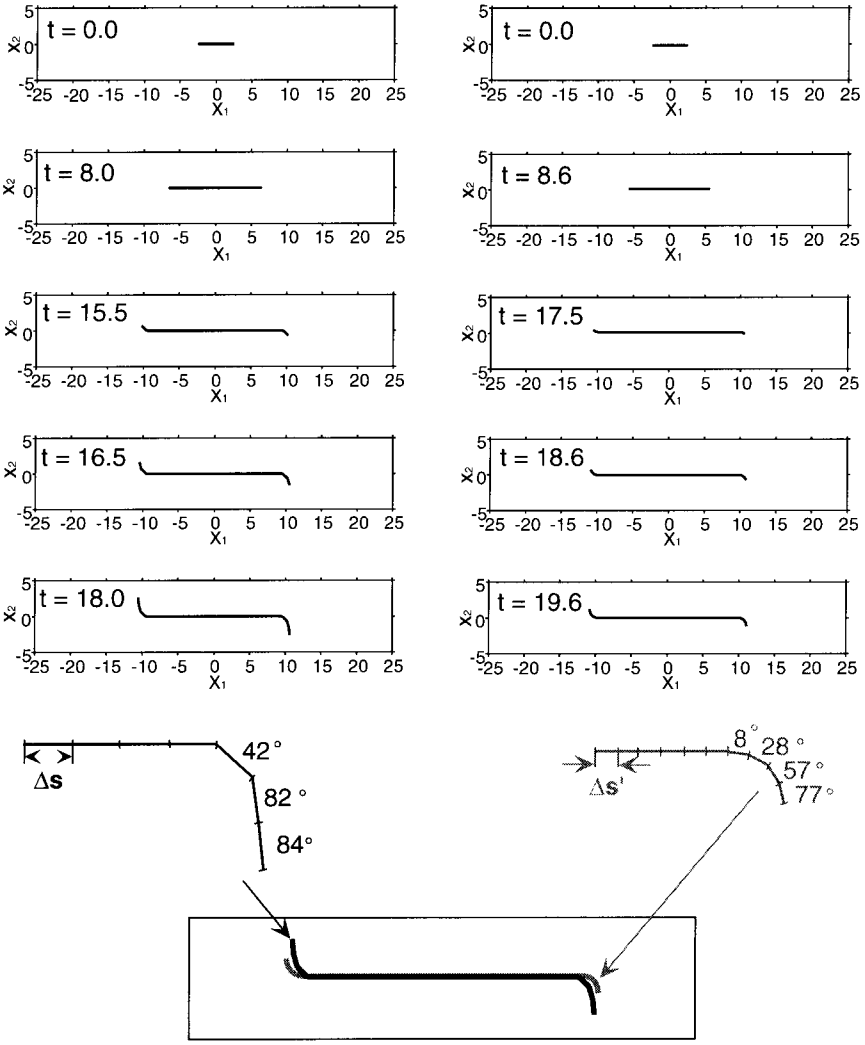

Figure 10. A comparison of two calculations with different resolutions. In the reference model of the left column, the length of a crack element and the increment of a time step are assumed to be $\Delta s = 1$ and $\Delta t = 0.5$. In the finely discretized model of the right column, $\Delta s' = (5/11)\Delta s$ and $\Delta t' = (5/11)\Delta t$ are assumed. The same initial crack lengths $l_0 = l'_0 = 5$ are assumed and they are discretized by 5 and 11 elements, respectively. The remotely applied stresses are also the same in the two models and their coefficients are set to be $\tau_0 = \tau'_0 = 1$. Note that a stress evaluation point ahead of a crack tip varies with an element length (see Fig. 1). Different values for the critical fracture strengths, $T_c = 1.21$ and $T'_c = 2.10$, are therefore determined even for the cracks with the same initial lengths and stress drops. The final crack lengths are $l_{stop} = 21.2$ and $l'_{stop} = 21.9$, which consist of 26 and 51 elements, respectively.

to carry out the simulation. Hypersingular boundary integral equations are derived first, and then the finite parts are taken to evaluate the hypersingular integrals. This greatly simplifies the analysis for the spontaneous growth of an arbitrarily oriented crack.

The crack tip was assumed to extend dynamically in the direction in which the hoop shear traction takes its maximum value and exceeds the fracture strength. Our simulation showed that the crack spontaneously bifurcates or bends at a high crack top velocity; the bending angle increases with the growth. The bending was interpreted to occur as a result of stress waves concentrated near the extending crack tip.

It was also shown that the crack tip growth is arrested soon after the onset of bending. This gives new insight into the arresting of earthquake rupture as discussed in Kame (1998) and Kame & Yamashita (1999). The arresting of earthquake faulting is generally supposed to occur through special inhomogeneities in the distributions of stress drop and/or fracture strength in prevailing theories (e.g. Das & Aki 1977b). Our simulations have shown that the crack growth can be arrested even in a uniformly stressed medium with homogeneously distributed fracture strengths.

The spontaneous arresting of crack tip growth is closely associated with the stress state on the bent branch of the crack. Once the bending angle at the crack tip exceeds a critical value, the shear traction released on the bent branch becomes negative, which causes a significant reduction in the crack tip stress concentration. This reduction finally arrests the crack tip growth.

We assumed a homogeneous elastic medium in this paper to elicit the crack dynamics. However, the Earth's crust is not necessarily homogeneous. In fact, fault zones are formed where larger earthquakes occur repeatedly; the fracture strength is believed to be lower in a fault zone than in the surrounding country rock. There may also be inhomogeneities in fracture strengths in a fault zone itself. These effects must be taken into account when applying our model to earthquake faulting. Some results of such consideration were discussed in Kame & Yamashita (1999); a more detailed analysis will be given in a subsequent paper.

The method developed in this paper can easily be applied to the analysis of more complex and realistic problems. One example is dynamic coalescence among cracks. The crack traces are expected to be strongly affected by waves reflected from each crack surface. The escape of the crack tip from inclusions with high fracture strength and a constitutive friction law on the crack surface may also be crucial elements to be investigated in further simulations.

ACKNOWLEDGMENTS

We are grateful to H. Fujiwara for advising us of the method of taking finite parts in evaluating the integrals having hypersingularities. Critical comments provided by J. Virieux and an anonymous reviewer led to significant revision of and improvement on our original manuscript. NK was supported by a Research Fellowship of the Japan Society for the Promotion of Science for Young Scientists, TY was supported in part by a Grant-in-Aid from the Ministry of Education, Science, Sports and Culture of Japan (project 08248111). Computation time was provided by the Supercomputer Center of the National Research Institute for Earth Science and Disaster Prevention.

REFERENCES

Aki, K. & Richards, P.G., 1980. *Quantitative Seismology—Theory and Methods,* Vol. 1, pp. 38–43, Freeman, New York.

Cochard, A. & Madariaga, R., 1994. Dynamic faulting under rate-dependent friction, *Pure appl. Geophys.,* **142,** 419–445.

Das, S., 1981. Three-dimensional spontaneous rupture propagation and implications for the earthquake source mechanism, *Geophys. J. R. astr. Soc.,* **67,** 375–393.

Das, S. & Aki, K., 1977a. A numerical study of two-dimensional spontaneous rupture propagation, *Geophys. J. R. astr. Soc.,* **50,** 643–668.

Das, S. & Aki, K., 1977b. Fault plane with barriers: a versatile earthquake model, *J. geophys. Res.,* **82,** 5658–5670.

Freund, L.B., 1990. *Dynamic Fracture Mechanics,* Cambridge University Press, Cambridge.

Fukuyama, E. & Madariaga, R., 1998. Rupture dynamics of a planar fault in a 3D elastic medium: rate- and slip-weakening friction, *Bull. seism. Soc. Am.,* **88,** 1–17.

Hadamard, J., 1923. *Lectures on Cauchy's Problem in Linear Partial Differential Equations,* Yale University Press, New Haven.

Imai, I., 1981. *Applied Hyperfunction Theory,* Science Press, Tokyo (in Japanese).

Inoue, T. & Miyatake, T., 1995. Computer simulation of dynamic source process on an arbitrary shaped fault, *Jpn. Earth planet. Sci. Joint Mg,* 361 (Japanese abstract).

Kame, N., 1998. Theoretical study on arresting mechanism of dynamic earthquake faulting, *DSc thesis,* University of Tokyo (in Japanese).

Kame, N. & Yamashita, T., 1997. Dynamic nucleation process of shallow earthquake faulting in a fault zone, *Geophys. J. Int.,* **128,** 204–216.

Kame, N. & Yamashita, T., 1999. A new light on arresting mechanism of dynamic earthquake faulting, *Geophys. Res. Lett.,* **26,** 1997–2000.

Kanamori, H., 1972. Determination of effective tectonic stress associated with earthquake faulting. The Tottori Earthquake of 1943, *Phys. Earth planet. Inter.,* **5,** 426–434.

Klees, R. & Lehmann, R., 1998. Calculation of strongly singular and hypersingular surface integrals, *J. Geodesy,* **72,** 530–546.

Koller, M.G., Bonnet, M. & Madariaga, R., 1992. Modelling of dynamical crack propagation using time-domain boundary integral equations, *Wave Motion,* **16,** 339–366.

Kostrov, B.V., 1964. Selfsimilar problems of propagation of shear cracks, *PMM J. appl. Math. Mech.,* **28,** 1077–1087.

Kostrov, B.V., 1966. Unsteady propagation of longitudinal shear cracks, *PMM J. appl. Math. Mech.,* **30,** 1241–1248.

Kostrov, B.V. & Das, S., 1988. *Principles of Earthquake Source Mechanics,* Cambridge University Press, Cambridge.

Madariaga, R., Olsen, K. & Archuleta, R., 1998. Modeling dynamic rupture in a 3D earthquake fault model, *Bull. seism. Soc. Am.,* **88,** 1182–1197.

Martin, P.A. & Rizzo, F.J., 1989. On boundary integral equations for crack problems, *Proc. R. Soc. Lond.,* A, **421,** 341–355.

Maruyama, T., 1966. On two-dimensional elastic dislocations in an infinite and semi-infinite medium, *Bull. Earthq. Res. Inst. Univ. Tokyo,* **44,** 811–871.

Matsuda, T., 1967. Geology of earthquake faults, *Zisin,* **20,** 230–235 (in Japanese).

Miyatake, T., 1980a. Numerical simulations of earthquake source process by a three-dimensional crack model. Part I. Rupture process, *J. Phys. Earth,* **28,** 565–598.

Miyatake, T., 1980b. Numerical simulations of earthquake source process by a three-dimensional crack model. Part II. Seismic waves and spectrum, *J. Phys. Earth,* **28,** 599–616.

Seelig, Th. & Gross, D., 1997. Analysis of dynamic crack propagation using a time-domain boundary integral equation method, *Int. J. Sol. Struct.,* **34,** 2087–2103.

Tada, T. & Yamashita, T., 1997. Non-hypersingular boundary integral equations for two-dimensional non-planar crack analysis, *Geophys. J. Int.,* **130,** 269–282.

Virieux, J. & Madariaga, R., 1982. Dynamic faulting studied by a finite difference method, *Bull. seism. Soc. Am.,* **72,** 345–369.

Xu, X.P. & Needleman, A., 1994. Numerical simulations of fast crack growth in brittle solids, *J. Mech. Phys. Sol.,* **42,** 1397–1434.

Yamashita, T. & Fukuyama, E., 1996. Apparent critical slip displacement caused by the existence of a fault zone, *Geophys. J. Int.,* **125,** 459–473.

Yoffe, E.H., 1951. The moving Griffith crack, *Phil. Mag.,* **42,** 739–50.

Zhang, Ch. & Achenbach, J.D., 1989. A new boundary integral equation formulation for elastodynamic and elastostatic crack analysis, *Trans. ASME J. appl. Mech.,* **56,** 284–290.

APPENDIX A: 2-D GREEN'S FUNCTIONS

The elastodynamic 2-D Green's functions are given by

$$G_{11}(\mathbf{x}, t-\tau; \mathbf{y}, 0) - G_{22}(\mathbf{x}, t-\tau; \mathbf{y}, 0)$$
$$= -\frac{1}{2\pi\mu}(\gamma_2^2-\gamma_1^2)\frac{\beta^2}{r^2}\left[2(t-\tau)^2-\frac{r^2}{\alpha^2}\right]\frac{1}{\sqrt{(t-\tau)^2-(r/\alpha)^2}}$$
$$\times H\left(t-\tau-\frac{r}{\alpha}\right)+\frac{1}{2\pi\mu}(\gamma_2^2-\gamma_1^2)\frac{\beta^2}{r^2}\left[2(t-\tau)^2-\frac{r^2}{\beta^2}\right]$$
$$\times\frac{1}{\sqrt{(t-\tau)^2-(r/\beta)^2}}H\left(t-\tau-\frac{r}{\beta}\right), \tag{A1}$$

$$G_{11}(\mathbf{x}, t-\tau; \mathbf{y}, 0) + G_{22}(\mathbf{x}, t-\tau; \mathbf{y}, 0)$$
$$=\frac{1}{2\pi\mu}\frac{\beta^2}{\alpha^2}\frac{1}{\sqrt{(t-\tau)^2-(r/\alpha)^2}}H\left(t-\tau-\frac{r}{\alpha}\right)$$
$$+\frac{1}{2\pi\mu}\frac{1}{\sqrt{(t-\tau)^2-(r/\beta)^2}}H\left(t-\tau-\frac{r}{\beta}\right), \tag{A2}$$

$$G_{12}(\mathbf{x}, t-\tau; \mathbf{y}, 0)=\frac{1}{2\pi\mu}\gamma_1\gamma_2\frac{\beta^2}{r^2}\left[2(t-\tau)^2-\frac{r^2}{\alpha^2}\right]$$
$$\times\frac{1}{\sqrt{(t-\tau)^2-(r/\alpha)^2}}H\left(t-\tau-\frac{r}{\alpha}\right)$$
$$-\frac{1}{2\pi\mu}\gamma_1\gamma_2\frac{\beta^2}{r^2}\left[2(t-\tau)^2-\frac{r^2}{\beta^2}\right]$$
$$\times\frac{1}{\sqrt{(t-\tau)^2-(r/\beta)^2}}H\left(t-\tau-\frac{r}{\beta}\right) \tag{A3}$$

(e.g. Tada & Yamashita 1997), where $r\equiv\|\mathbf{x}-\mathbf{y}\|$, $\gamma_i\equiv(x_i-y_i)/r$, and $H(\cdot)$ is the Heaviside step function. α and β denote the *P*- and *S*-wave velocities, respectively.

Note that the expression

$$\frac{\beta^2}{r^2}\left(\frac{1}{\sqrt{(t-\tau)^2-(r/\alpha)^2}}-\frac{1}{\sqrt{(t-\tau)^2-(r/\beta)^2}}\right) \tag{A4}$$

converges to a finite limit value as $r\to 0$, so that the elastodynamic Green's functions that contain this expression are not hypersingular at $r=0$.

The elastostatic 2-D Green's functions are given by

$$G_{11}(\mathbf{x}; \mathbf{y}) - G_{22}(\mathbf{x}; \mathbf{y}) = \frac{1}{4\pi\mu}\left[-\left(1-\frac{\beta^2}{\alpha^2}\right)(\gamma_2^2-\gamma_1^2)\right], \tag{A5}$$

$$G_{11}(\mathbf{x}; \mathbf{y}) + G_{22}(\mathbf{x}; \mathbf{y}) = \frac{1}{4\pi\mu}\left[\left(1-\frac{\beta^2}{\alpha^2}\right)-2\left(1+\frac{\beta^2}{\alpha^2}\right)\log r\right], \tag{A6}$$

$$G_{12}(\mathbf{x}, \mathbf{y}) = \frac{1}{4\pi\mu}\left(1-\frac{\beta^2}{\alpha^2}\right)\gamma_1\gamma_2 \tag{A7}$$

(e.g. Maruyama 1966; Zhang & Achenbach 1989).

APPENDIX B: FINITE PART OF THE DIVERGENT INTEGRAL

The divergent integrals appearing in the BIEM have the form

$$\int_a^b \frac{f(t)}{(b^2-t^2)^{3/2}}dt \quad (a<b), \tag{B1}$$

where $t=b$ is the hypersingular point at the wave front. This is to be evaluated by taking a finite part (Martin & Rizzo 1989). We can distinguish a finite part and a divergent part taking the limit $\varepsilon\to+0$:

$$\int_a^{b-\varepsilon}\frac{f(t)}{(b^2-t^2)^{3/2}}dt$$
$$=-\int_a^{b-\varepsilon}\frac{f(b)-f(t)}{(b^2-t^2)^{3/2}}dt+f(b)\int_a^{b-\varepsilon}\frac{dt}{(b^2-t^2)^{3/2}}$$
$$=-\int_a^{b-\varepsilon}\frac{f(b)-f(t)}{(b^2-t^2)^{3/2}}dt-\frac{a}{b^2}\frac{f(b)}{\sqrt{b^2-a^2}}+\frac{1}{\sqrt{\varepsilon}}\frac{(b-\varepsilon)f(b)}{b^2\sqrt{2b-\varepsilon}}, \tag{B2}$$

then

$$\text{p.f.}\int_a^b\frac{f(t)}{(b^2-t^2)^{3/2}}dt\equiv-\int_a^b\frac{f(b)-f(t)}{(b^2-t^2)^{3/2}}dt-\frac{a}{b^2}\frac{f(b)}{\sqrt{(b^2-a^2)}}. \tag{B3}$$

This is the finite part of the diverent integral first defined by Hadamard (1923). This definition has the advantage that we can take the finite part for any regular function $f(t)$ even if the primitive function of the integral on the right-hand side of eq. (B3) does not exist. In that case, the finite part on the right-hand side should be evaluated numerically, but it is usually cumbersome because 0/0 will appear in the integrand as $t\to b$. The usefulness of methods based on finite-part integrals was also confirmed by Klees & Lehmann (1998). They developed some effective computation methods for the numerical evaluation of the finite part of a typical hypersingular integral appearing in the field of geodesy.

In this paper, we introduce a more useful and direct definition for the finite part with the aid of hyperfunction theory (e.g. Imai 1981):

$$\text{p.f.}\int_0^a x^\alpha\varphi(x)dx\equiv\int_{-\varepsilon}^a\varphi(x)|x|^\alpha H(x)dx. \tag{B4}$$

The integral $\int_0^a$ on the left-hand side generally contains a hypersingularity at $x=0$ for $\alpha<-1$, so that it is divergent in

the classical sense. The divergent part is, however, removed by this definition automatically because the hypersingularity at $x=0$ is eliminated by $H(x)$ at $x=-\varepsilon$ [because $H(-\varepsilon)=0$]. It can be easily proved that the application of the definition (B4) to the evaluation of the integral (B1) yields a result identical to that given in eq. (B3). It is analytically demonstrated that the definition (B4) is equivalent to Hadamard's one for any degree of hypersingularity (Imai 1981). Although the definition (B4) is for one-side divergent integrals, it can be extended for both-side divergent integrals (of course, including the case of the Cauchy principal value for $\alpha=-1$). In our problem, such both-side integrals appear at $r=0$ in the static problem, where r is the distance between the observation point and the source point (Appendix C). the stress operators (eq. 17 and eq. C7) can be directly evaluated by eq. (B4) without numerical integration.

APPENDIX C: SOLUTION FOR STATIC SLIP

In the static problem, the representation theorem for the displacement field holds in the form that does not include time dependence. Application of Hooke's law leads to the following representation for the stress field:

$$\begin{aligned}\frac{1}{2}[\sigma_{11}(\mathbf{x})-\sigma_{22}(\mathbf{x})] &= -\text{p.f.}\int_\Gamma d\xi \Delta u_t(\xi)\mu^2\left\{2n_1(\xi)n_2(\xi)\right.\\ &\times\left(\frac{\partial^2}{\partial x_1^2}G_{11}+\frac{\partial^2}{\partial x_2^2}G_{22}-2\frac{\partial^2}{\partial x_1\partial x_2}G_{12}\right)+[n_2^2(\xi)-n_1^2(\xi)]\\ &\times\left.\left[\frac{\partial^2}{\partial x_1\partial x_2}(G_{11}-G_{22})+\left(\frac{\partial^2}{\partial x_1^2}-\frac{\partial^2}{\partial x_2^2}\right)G_{12}\right]\right\},\end{aligned} \tag{C1}$$

$$\begin{aligned}\frac{1}{2}[\sigma_{11}(\mathbf{x})+\sigma_{22}(\mathbf{x})] &= -\text{p.f.}\int_\Gamma d\xi \Delta u_t(\xi)\mu(\lambda+\mu)\left\{2n_1(\xi)n_2(\xi)\right.\\ &\times\left(\frac{\partial^2}{\partial x_1^2}G_{11}-\frac{\partial^2}{\partial x_2^2}G_{22}\right)+[n_2^2(\xi)-n_1^2(\xi)]\\ &\times\left.\left[\frac{\partial^2}{\partial x_1\partial x_2}(G_{11}+G_{22})+\left(\frac{\partial^2}{\partial x_1^2}+\frac{\partial^2}{\partial x_2^2}\right)G_{12}\right]\right\},\end{aligned} \tag{C2}$$

$$\begin{aligned}\sigma_{12} = -\text{p.f.}\int_\Gamma d\xi \Delta u_t(\xi,\tau)\mu^2&\left\{2n_1(\xi)n_2(\xi)\right.\\ &\times\left[\frac{\partial^2}{\partial x_1\partial x_2}(G_{11}-G_{22})+\left(\frac{\partial^2}{\partial x_1^2}-\frac{\partial^2}{\partial x_2^2}\right)G_{22}\right]\\ &+\left.[n_2^2(\xi)-n_1^2(\xi)]\left(\frac{\partial^2}{\partial x_2^2}G_{11}+\frac{\partial^2}{\partial x_1^2}G_{22}+2\frac{\partial^2}{\partial x_1\partial x_2}G_{12}\right]\right\},\end{aligned} \tag{C3}$$

where the static stress components are related to the static right-lateral slip in the crack using the notation of eq. (4).

With the limiting process $\mathbf{x}\to\mathbf{y}(s)$, we have the tractions, $T_t(s)$ and $T_n(s)$, on the crack at arc length s:

$$\begin{aligned}T_t(s) &= 2n_1(s)n_2(s)\frac{1}{2}[\sigma_{11}(\mathbf{y}(s)]-\sigma_{22}(\mathbf{y}(s)))\\ &+[n_2^2(s)-n_1^2(s)]\sigma_{12}(\mathbf{y}(s)),\end{aligned} \tag{C4}$$

$$\begin{aligned}T_n(s) &= \frac{1}{2}[\sigma_{11}(\mathbf{y}(s)]+\sigma_{22}(\mathbf{y}(s)))\\ &-[n_2^2(s)-n_1^2(s)]\frac{1}{2}[\sigma_{11}(\mathbf{y}(s))-\sigma_{22}(\mathbf{y}(s))]\\ &+2n_1(s)n_2(s)\sigma_{12}(\mathbf{y}(s)).\end{aligned} \tag{C5}$$

As in the dynamic case, the crack is represented by discrete boundary elements with equal length Δs, and a piecewise constant interpolation function is used. Then the stress components are represented in a discrete form:

$$\begin{aligned}\sigma_{ij}(\mathbf{x}) &= \text{p.f.}\int_\Gamma \Delta u_t(\xi)\frac{\partial^2}{\partial x_p\partial x_q}G\,d\xi\\ &= \sum_i D^i\,\text{p.f.}\int_{s_i}^{s_{i+1}}\frac{\partial^2}{\partial x_p\partial x_q}G\,d\xi\\ &= \sum_i D^i I^i_{\text{static}}(\mathbf{x}),\end{aligned} \tag{C6}$$

with

$$I^i_{\text{static}}(\mathbf{x}) = \text{p.f.}\int_{s_i}^{s_{i+1}}\frac{\partial^2}{\partial x_p\partial x_q}G\,d\xi, \tag{C7}$$

where D^i is the discretized static slip on the ith element, $I^i_{\text{static}}(\mathbf{x})$ is the static stress operator that relates the stress at the position $\mathbf{x}$ and the slip on ith element. In the static case, hypersingularities of order $1/r^2$ appear in the kernel functions $\partial^2 G/\partial x_p\partial x_q$ at $r=0$, which are evaluated by taking the finite parts.

For the boundary integral eq. (C4), the traction is evaluated at the centre of each discretized element and we obtain a set of simultaneous equations on Γ:

$$T_t^l = \sum_i^{m_0} D^i K^{l-i}_{\text{static}}, \tag{C8}$$

where m_0 is the number of discrete elements on Γ, and K^{l-i}_{static} is a traction operator composed of the stress components and the normal vector.

We use eq. (C8) for the determination of the static slips D^i on the seed crack that are in an equilibrium state with stress drop $\Delta\sigma$. Once the static slips on the seed crack are determined, the static stress field can be calculated using eqs (C1), (C2) and (C3).

APPENDIX D: LOAD FOR EACH FRACTURE MODE

In this paper, we investigated the dynamic growth of in-plane shear cracks (mode II), and found spontaneous bending and arresting. Here the possibility of self-stopping is discussed for the other fracture modes, an in-plane tensile crack (mode I) and anti-plane crack (mode III), in terms of a remotely applied load.

For each mode, Freund (1990) derived analytical solutions of the singular terms of stresses at the crack tip growing with velocity v. The hoop tractions associated with each fracture

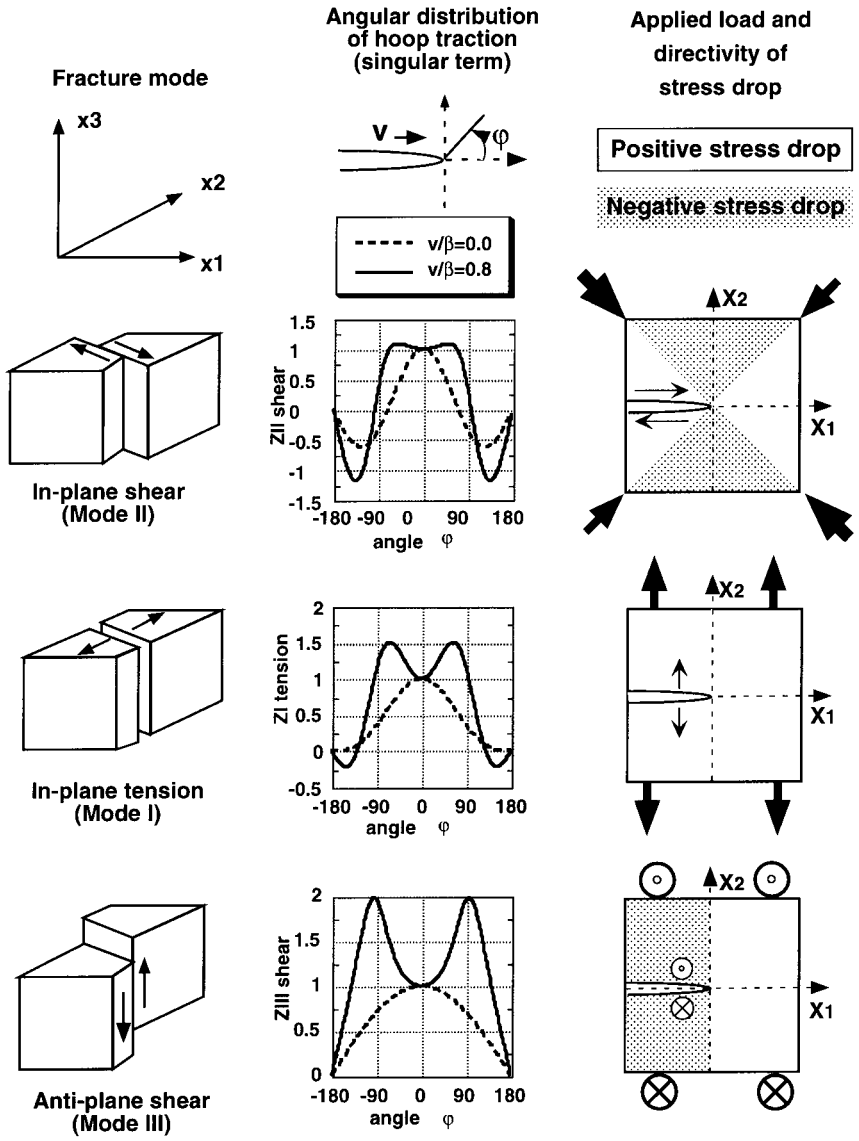

Figure D1. Three types of fracture modes, hoop traction distributions and their remotely applied loads. (a) in-plane shear (mode II), (b) in-plane tension (mode I), and (c) anti-plane shear (mode III).

mode can be constructed from them. The tractions that we consider here are tensile for mode I and shear for mode III. The angular distributions of the hoop tractions are shown in Fig. D1. That of mode II is also plotted as a reference. The maximum hoop tractions are all in the direction $\varphi = 0^\circ$ in the static state $v = 0$, the original crack plane. The maximum directions, however, shift from the original plane with $v = 0.8\beta$ in all modes. The critical velocity across which the maximum axis begins to shift from the original plane is also found by use of the analytical solutions. The critical velocities v^c are $v_I^c = 0.62\beta$, $v_{II}^c = 0.77\beta$ and $v_{III}^c = 80.44\beta$ for modes I, II and III, respectively. The difference among modes is inferred from the different radiation patterns of stress waves. It can be concluded from Freund's solutions that a fast-growing crack is expected to bend spontaneously in all modes.

The possibility of spontaneous arresting is governed by the boundary condition on the curved crack surface. The remotely applied load that leads each fracture mode is also shown in Fig. D1. The seed cracks are located along the X_1-axis, where the maximum stress drop occurs. The angular pattern of stress drop for the forthcoming curved crack surface is shown. The white and grey ranges represent the positive and negative stress drop, respectively. As stated in this paper, the mode II crack tip enters the region where the negative stress drop occurs, which bring about a significant decrease of the stress concentration at the crack tip. For mode I cracking, the possibility of negative stress drop does not exist. Thus the dynamic crack growth cannot be spontaneously arrested for a homogeneous distribution of fracture strength and uniformly applied load. In the mode III case, the negative stress drop can occur on the curved crack surface if the bending angle exceeds a critical angle $\varphi = 90^\circ$. Further simulations are necessary to verify the possibility of the self-arresting of spontaneous crack growth for mode III.